

## Supporting Information

### **Robust coherent spin centers from stable azafullerene radicals entrapped in cycloparaphenylene rings**

*Yuri Tanuma, Anastasios Stergiou, Andreja Bužan Bobnar, Mattia Gaboardi, Jeremy Rio, Jannis Volkmann, Hermann A. Wegner, Nikos Tagmatarchis, Christopher P. Ewels,\* Denis Arčon\**

Y. Tanuma

Institut des Matériaux Jean Rouxel, CNRS / Université de Nantes, BP32229, 44322 Nantes, France

Graduate School of Interdisciplinary New Science, Toyo University, 2100 Kujirai, Kawagoe, 350-8585, Saitama, Japan

Dr. A. Stergiou, Prof. N. Tagmatarchis

Theoretical and Physical Chemistry Institute, National Hellenic Research Foundation, 48 Vassileos Constantinou Avenue, 11635 Athens, Greece

A. B. Bobnar

Jožef Stefan Institute, Jamova 39, 1000 Ljubljana, Slovenia

Dr. M. Gaboardi

Sincrotrone Trieste S.C.p.A., Strada Statale 14 Km 163.5, I-34149 Trieste, Italy

Jannis Volkmann, Prof. Dr. H. A. Wegner

Institute of Organic Chemistry, Justus Liebig University Giessen, Heinrich-Buff-Ring 17, 35392, Giessen, Germany

Center for Materials Research (LaMa), Justus Liebig University Giessen, Heinrich-Buff-Ring 16, 35392, Giessen, Germany

Dr J. Rio, Dr. C. P. Ewels

Institut des Matériaux Jean Rouxel, CNRS / Université de Nantes, BP32229, 44322 Nantes, France

E-mail: [chris.ewels@cnrs-immn.fr](mailto:chris.ewels@cnrs-immn.fr)

Prof. D. Arčon

Jožef Stefan Institute, Jamova 39, 1000 Ljubljana, Slovenia.

Faculty of Mathematics and Physics, University of Ljubljana, Jadranska 19, 1000 Ljubljana, Slovenia.

E-mail: [denis.arcon@ijs.si](mailto:denis.arcon@ijs.si)

### [10]CPP $\supset$ (C<sub>59</sub>N)<sub>2</sub> $\subset$ [10]CPP sample preparation and crystallographic characterization

Powder samples of [10]CPP $\supset$ (C<sub>59</sub>N)<sub>2</sub> $\subset$ [10]CPP were prepared following an analogous procedure as that employed to prepare C<sub>60</sub>@[10]CPP powders<sup>1,2</sup> and were thoroughly characterized to confirm the presence of azafullerenes and of [10]CPP rings in the sample.

Powder synchrotron X-ray diffraction of the as-prepared sample, measured on the X-ray powder diffraction beamline MCX at Elettra (Trieste, Italy),<sup>3</sup> shows broadened diffraction peaks (Fig. S1) that could not be indexed to any of the known pure [10]CPP, (C<sub>59</sub>N)<sub>2</sub> or C<sub>60</sub> $\subset$ [10]CPP crystal structures. Although common methods from fullerene chemistry (i.e. slow-evaporation, vapor diffusion) have been utilized to promote the formation of single crystals of the [10]CPP $\supset$ (C<sub>59</sub>N)<sub>2</sub> $\subset$ [10]CPP complex, taking into consideration the dimer nature of (C<sub>59</sub>N)<sub>2</sub> and the related orientational disorder of the material<sup>4</sup> -in contrast to C<sub>60</sub>- it is reasonable to face difficulty in obtaining a disorder-free single crystal material. We should, however, mention that all studied powders of the [10]CPP $\supset$ (C<sub>59</sub>N)<sub>2</sub> $\subset$ [10]CPP complex have the same XRD pattern as shown in **Figure S1**.

The strongest peaks in the pattern suggest a low symmetry (most likely triclinic or monoclinic), possibly derived through various subgroups relations from the distortion of a parent large cubic cell (of about 4.2 nm extension). By applying Le Bail pattern decomposition, we temporarily indexed our data to a monoclinic unit cell with lattice parameters  $a = 2.75044$  nm,  $b = 2.89104$  nm,  $c = 3.89104$  nm, and  $\beta = 97.396^\circ$ , consistent with 8 structural units. Albeit beyond the scope of this paper, further syntheses optimized for powder diffraction investigation are in progress and will hopefully address the structural problem. The unit cell volume of 30.683 nm<sup>3</sup> thus appears significantly expanded by a factor of  $\sim 15.9$  compared to the unit cell comprising a herringbone arrangement of C<sub>60</sub> $\subset$ [10]CPP<sup>1</sup> or (C<sub>59</sub>N)<sub>2</sub><sup>5</sup> solid. Such large expansion is probably a direct consequence of the dimer structure of diamagnetic [10]CPP $\supset$ (C<sub>59</sub>N)<sub>2</sub> $\subset$ [10]CPP basic building blocks. The small number of peaks and low peak intensity do not allow us to perform more detailed Rietveld refinement and to extract the packing of individual [10]CPP $\supset$ (C<sub>59</sub>N)<sub>2</sub> $\subset$ [10]CPP entities in the monoclinic unit cell. Nonetheless the present powder synchrotron X-ray diffraction confirms that it is possible to crystallize [10]CPP $\supset$ (C<sub>59</sub>N)<sub>2</sub> $\subset$ [10]CPP to a phase pure sample, thus opening a route to address its electronic state.

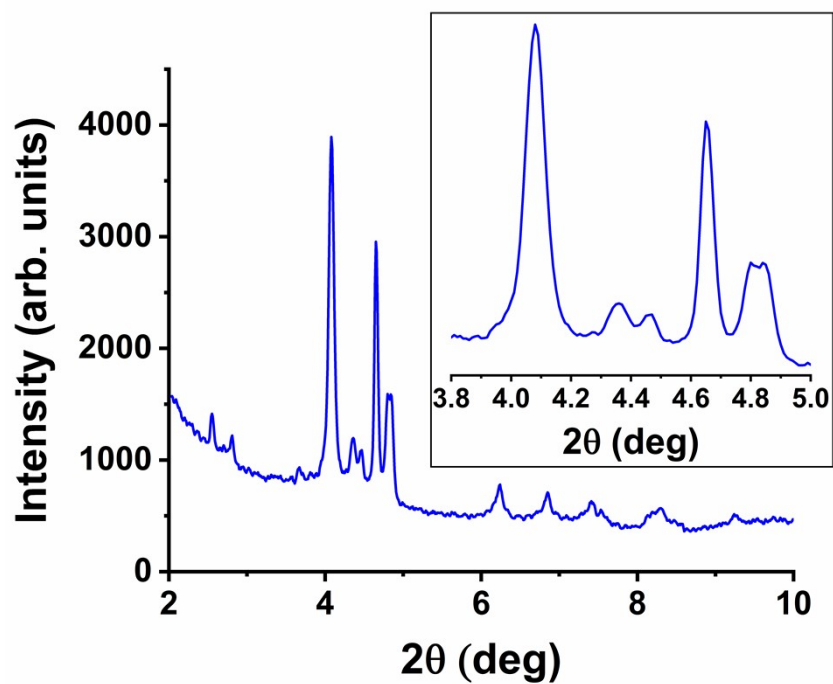


**Figure S1.**

The powder synchrotron X-ray diffraction profile of [10]CPP⊃(C<sub>59</sub>N)<sub>2</sub>⊂[10]CPP measured at room temperature.  $\lambda = 0.10332$  nm.

### [10]CPP $\supset$ (C<sub>59</sub>N)<sub>2</sub> $\subset$ [10]CPP characterization by FT-IR and Raman spectroscopy.

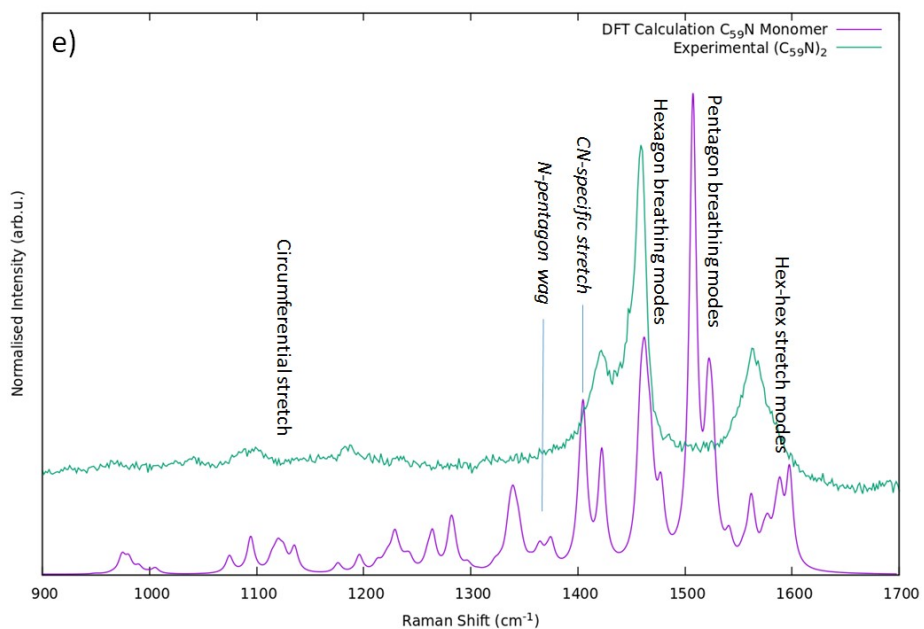
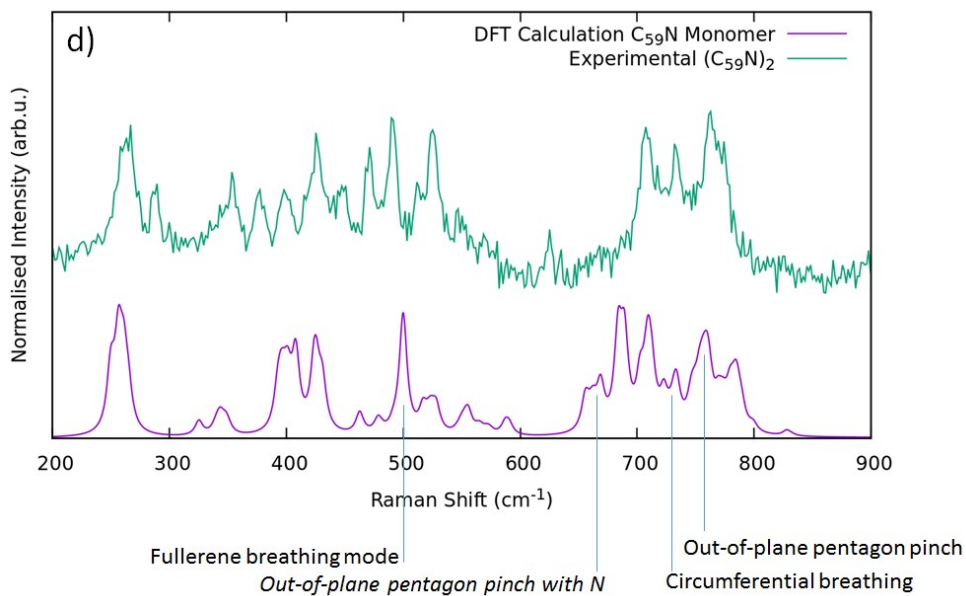
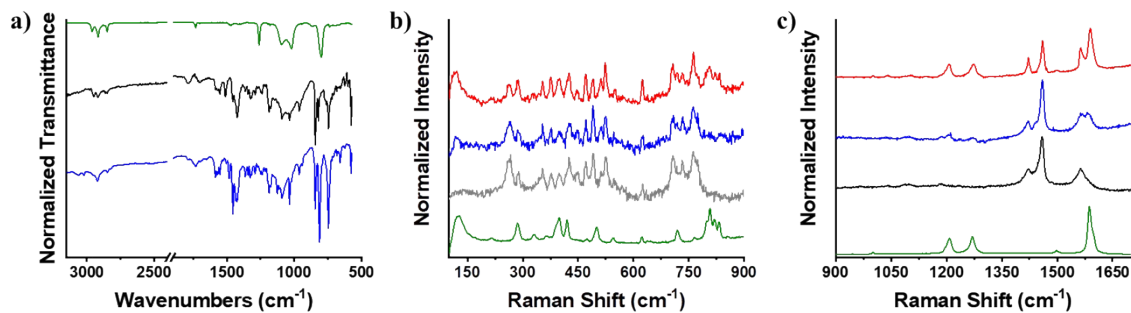
The FT-IR spectrum (**Figure S2a**) of the [10]CPP $\supset$ (C<sub>59</sub>N)<sub>2</sub> $\subset$ [10]CPP complex shows an overlap of the spectra of the individual components ([10]CPP and (C<sub>59</sub>N)<sub>2</sub>), at first glance. Pristine (C<sub>59</sub>N)<sub>2</sub> shows two distinct signals at 819 and 843 cm<sup>-1</sup> related to its dimer nature,<sup>6</sup> while [10]CPP has intense bands at 800 (characteristic of out-of-plane C-H deformation from a para-disubstituted benzene ring vibration), 1017 and 1091 (in-plane C-H bending) and 2920 cm<sup>-1</sup> (C-H stretching), analogous to benzene derivatives. The spectrum of the as-prepared [10]CPP $\supset$ (C<sub>59</sub>N)<sub>2</sub> $\subset$ [10]CPP complex shows the distinct signals of the azafullerene dimer within the complex at 811 (8 cm<sup>-1</sup> downshift, as compared to the non-complexed dimer) and 843 cm<sup>-1</sup>. Furthermore, the in-plane C-H bending modes of the [10]CPP nanobelts hosting the dimer were found at 1020 (3 cm<sup>-1</sup> upshift, as compared to the empty [10]CPP), while the second mode is probably masked or with decreased intensity. Decreased intensity of the 1090 cm<sup>-1</sup> has been observed in 1D-aligned cycloparaphenylenes by covalent means.<sup>7</sup> Interestingly, for the [10]CPP $\supset$ (C<sub>59</sub>N)<sub>2</sub> $\subset$ [10]CPP complex the band of the C-H stretching at 2920 cm<sup>-1</sup> is accompanied by the evolution of flanking bands at 3020 cm<sup>-1</sup>, also reported for 1D-aligned cycloparaphenylenes.

Raman spectroscopy (**Figure S2b,c**) shed more light into the structure of the [10]CPP $\supset$ (C<sub>59</sub>N)<sub>2</sub> $\subset$ [10]CPP complex, both in the as-prepared state but also after the thermal annealing treatment. For pristine [10]CPP, characteristic bands are present at 125 (cycloparaphenylene's radial breathing mode), 1270 (distortion and deformation of the benzene units in the individual benzene planes or cycloparaphenylene's D band) and 1587 cm<sup>-1</sup> (C<sub>ortho</sub>-C<sub>ortho</sub> stretching or cycloparaphenylene's G band),<sup>8</sup> while for pristine (C<sub>59</sub>N)<sub>2</sub> the radial breathing mode of the azafullerene cage at 490 cm<sup>-1</sup> and the pentagonal pinch mode of the cage at 1458 cm<sup>-1</sup> are also evident. The as-prepared [10]CPP $\supset$ (C<sub>59</sub>N)<sub>2</sub> $\subset$ [10]CPP complex shows the following characteristic modes: the 121 cm<sup>-1</sup> RBM mode (downshifted by 4 cm<sup>-1</sup> as compared to pristine [10]CPP), the radial breathing mode of the azafullerene cage at 490 cm<sup>-1</sup> and the pentagonal pinch mode of the cage at 1458 cm<sup>-1</sup> (no differences found as compared to the pristine azafullerene dimer) and the 1270 and 1587 cm<sup>-1</sup> modes (no differences found as compared to pristine [10]CPP). The downshifted RBM mode in the spectrum of [10]CPP $\supset$ (C<sub>59</sub>N)<sub>2</sub> $\subset$ [10]CPP complex is possibly due to the encapsulation of the azafullerene cages within the [10]CPP nanobelts (analogous findings were reported for C<sub>60</sub>@SWNT peapods<sup>9</sup>). Further, the thermally treated complex resembles the profile of the non-treated complex, however, shifts in the position of some bands was witnessed. Specifically, the thermally treated [10]CPP $\supset$ (C<sub>59</sub>N)<sub>2</sub> $\subset$ [10]CPP complex has the following characteristic modes:

the 117 cm<sup>-1</sup> RBM mode (downshifted by 8 cm<sup>-1</sup> as compared to pristine [10]CPP), the RBM of the azafullerene cage at 490 cm<sup>-1</sup> (no difference found as compared to the pristine azafullerene dimer), the pentagonal pinch mode of the cage at 1460 cm<sup>-1</sup> (upshifted by 2 cm<sup>-1</sup> as compared to the pristine azafullerene dimer), the 1274 cm<sup>-1</sup> mode (upshifted by 4 cm<sup>-1</sup> as compared to pristine [10]CPP) and the 1590 cm<sup>-1</sup> mode (upshifted by 3 cm<sup>-1</sup> as compared to pristine [10]CPP).

The 2 cm<sup>-1</sup> upshift for the pentagonal pinch mode in the thermally-treated [10]CPP $\supset$ (C<sub>59</sub>N)<sub>2</sub> $\subset$ [10]CPP complex could be related to the loss of electron density due to the transformation to the paramagnetic C<sub>59</sub>N<sup>•</sup> $\subset$ [10]CPP species (see also the case of C<sub>59</sub>N<sup>+</sup>,<sup>10</sup> upshift of 7 cm<sup>-1</sup> moving from the neutral dimer to the C<sub>59</sub>N<sup>+</sup>) and further related to the 4 cm<sup>-1</sup> upshift of the G band of the [10]CPP host, indicating charge doping effects, likewise the case of charge doping in carbon nanotubes.

DFT calculations using the Plaszczek approximation to calculate Raman intensities, with an excitation energy of 1.9eV, show good qualitative agreement between the calculated C<sub>59</sub>N monomer spectrum and the experimental as-prepared (C<sub>59</sub>N)<sub>2</sub> spectrum. Notably there are some calculated peaks (labelled in italics) not visible in the experimental data specifically concerned with vibrations at least partially localized on the nitrogen atom and its neighbours. As such these may serve as indicators of the presence of the radical monomer. However they are not visible in the thermally treated spectrum since the radical is a minority species and the signal to noise ratio is not sufficient to identify the peaks.



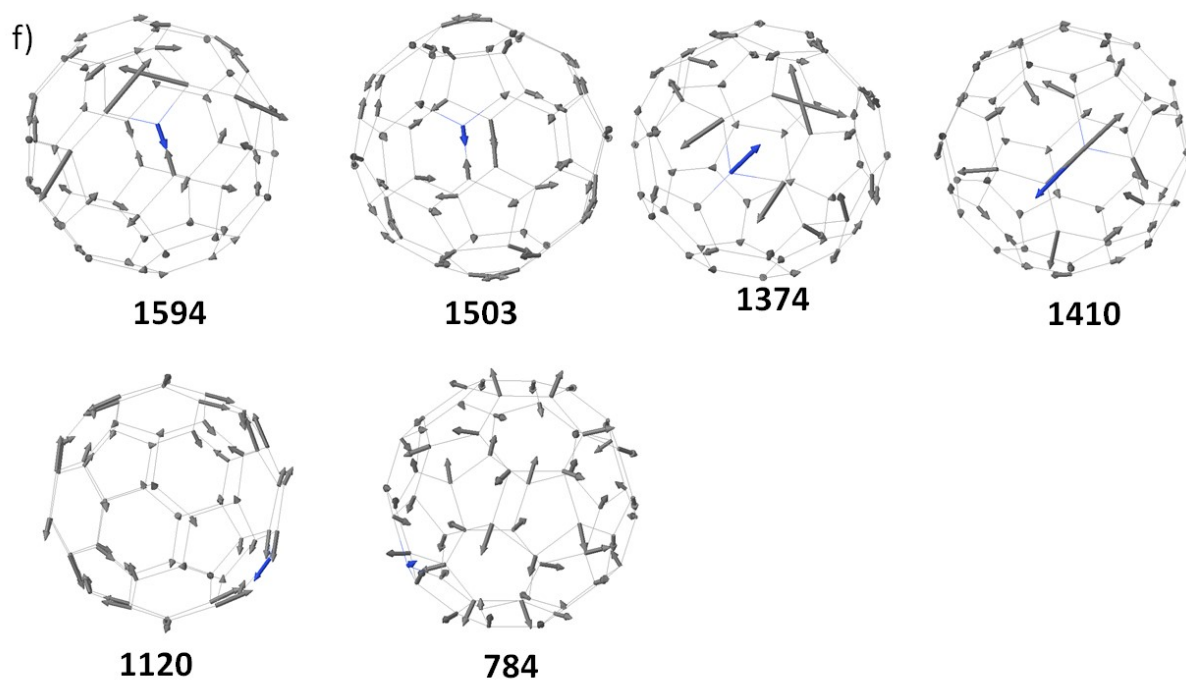


**Figure S2.**

(a) FT-IR spectra of [10]CPP (green line),  $(C_{59}N)_2$  (black line) and the [10]CPP $\supset(C_{59}N)_2\subset$ [10]CPP complex (blue line), recorded via an ATR accessory at ambient conditions. (b, c) Raman spectra of [10]CPP (green line),  $(C_{59}N)_2$  (black line), the as-prepared [10]CPP $\supset(C_{59}N)_2\subset$ [10]CPP complex (blue line) and the thermally-treated [10]CPP $\supset(C_{59}N)_2\subset$ [10]CPP complex (red line). Raman spectra were recorded at 633 nm (<0.3 mW), at room temperature via a long 50x focus lens. All samples were in powder form. The thermally-treated [10]CPP $\supset(C_{59}N)_2\subset$ [10]CPP powder (red line) was measured through the vacuum-sealed 4 mm diameter silica EPR tube (Wilmad Lab Glass). (d,e) Comparison of the  $(C_{59}N)_2$  as-prepared dimer Raman spectrum with DFT-calculated spectrum for an isolated  $C_{59}N$  radical monomer (intensities generated using Plasczek approximation) at 1.9eV excitation energy. Labels describe key features, italics indicates a feature involving significant motion of the nitrogen. (f) Eigenvectors of key vibrational modes (frequencies listed in  $cm^{-1}$ ), notably highlighting modes localized on the nitrogen and neighbours. The nitrogen atom eigenvector is marked in blue, while carbon atom eigenvectors are marked in grey.

## NMR Measurements

Solid state  $^1\text{H}$  and  $^{13}\text{C}$  magic angle spinning (MAS) NMR measurements at room temperature on as-prepared samples for reference samples [10]CPP,  $(\text{C}_{59}\text{N})_2$  and [10]CPP $\supset$ ( $\text{C}_{59}\text{N}$ ) $_2$  $\subset$ [10]CPP powders further confirm the interaction between the  $\text{C}_{59}\text{N}$  and [10]CPP host nanohoops. The representative room temperature spectra of as-prepared samples are shown in **Figure S3** (the  $^{13}\text{C}$  NMR signal from the tiny Teflon tape has been also seen at around 110 ppm and is not shown here).  $^{13}\text{C}$  MAS NMR spectrum of [10]CPP powder (green line) comprises two main peaks at 127.8 and 137.3 ppm, the first corresponding to C-atoms coupled to H and the second to quaternary C-atoms connecting the phenyl rings. On the other hand,  $^{13}\text{C}$  MAS peaks of  $(\text{C}_{59}\text{N})_2$  are mostly concentrated between 140 and 150 ppm (blue line), as expected for a fullerene molecule. When  $\text{C}_{59}\text{N}$  is encapsulated by [10]CPP in [10]CPP $\supset$ ( $\text{C}_{59}\text{N}$ ) $_2$  $\subset$ [10]CPP, all peaks slightly shift (black line). The largest changes are seen for the  $(\text{C}_{59}\text{N})_2$ , for example, the peak at 141.7 ppm shifts to 143.3 ppm, reflecting the confined environment after encapsulation. Importantly, the measured spectrum is not just simply a sum of those measured on [10]CPP and  $(\text{C}_{59}\text{N})_2$  compositions (red line) as the  $^{13}\text{C}$  NMR signal intensity is significantly redistributed over entire frequency span.

$^1\text{H}$  MAS NMR spectra measured on [10]CPP reference and [10]CPP $\supset$ ( $\text{C}_{59}\text{N}$ ) $_2$  $\subset$ [10]CPP are compared in the figure below (peaks between 1 and 2 ppm arise from the minute amount of impurities attached to the Teflon tape). The spinning frequency was 35 kHz. As hydrogen atoms are distanced from the encapsulated azafullerene molecules, the effects appear subtler, but are nevertheless visible in the small shift and the narrowing of the signal. Literature studies of biphenyl confirm NMR shifts with the torsional angle of neighbouring phenyl groups,<sup>11</sup> and this is consistent with the signal narrowing in the case of [10]CPP $\supset$ ( $\text{C}_{59}\text{N}$ ) $_2$  $\subset$ [10]CPP, as fullerene encapsulation restricts the torsional flexing of the phenyl groups in its encapsulating [10]CPP.

Both  $^1\text{H}$  and  $^{13}\text{C}$  MAS NMR spectra of [10]CPP $\supset$ ( $\text{C}_{59}\text{N}$ ) $_2$  $\subset$ [10]CPP powders show changes with respect to reference [10]CPP and  $(\text{C}_{59}\text{N})_2$  samples and clearly speak for the interaction between the [10]CPP and  $(\text{C}_{59}\text{N})_2$  at the molecular level. As such, they thus provide additional independent evidence for the encapsulation of  $\text{C}_{59}\text{N}$  by the [10]CPP.

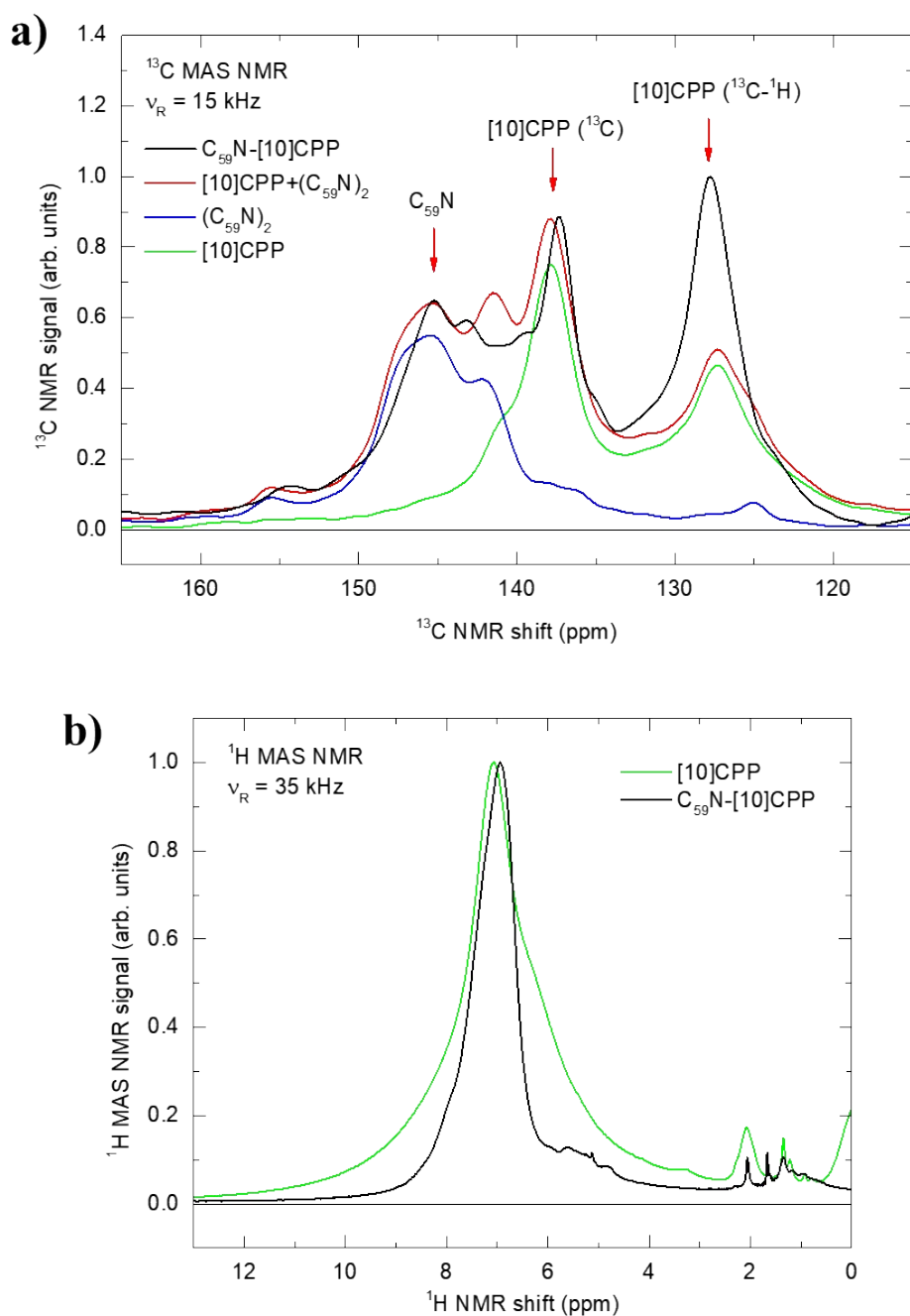


**Figure S3.**

Solid state (a)  $^{13}\text{C}$  and (b)  $^1\text{H}$  MAS NMR measurements on reference samples [10]CPP (green lines), ( $\text{C}_{59}\text{N}$ )<sub>2</sub> (blue lines) and [10]CPP-( $\text{C}_{59}\text{N}$ )<sub>2</sub>-[10]CPP (black lines) powders. The red line in (a) is a sum of [10]CPP and ( $\text{C}_{59}\text{N}$ )<sub>2</sub>  $^{13}\text{C}$  MAS NMR spectra to be compared with that of [10]CPP-( $\text{C}_{59}\text{N}$ )<sub>2</sub>-[10]CPP.

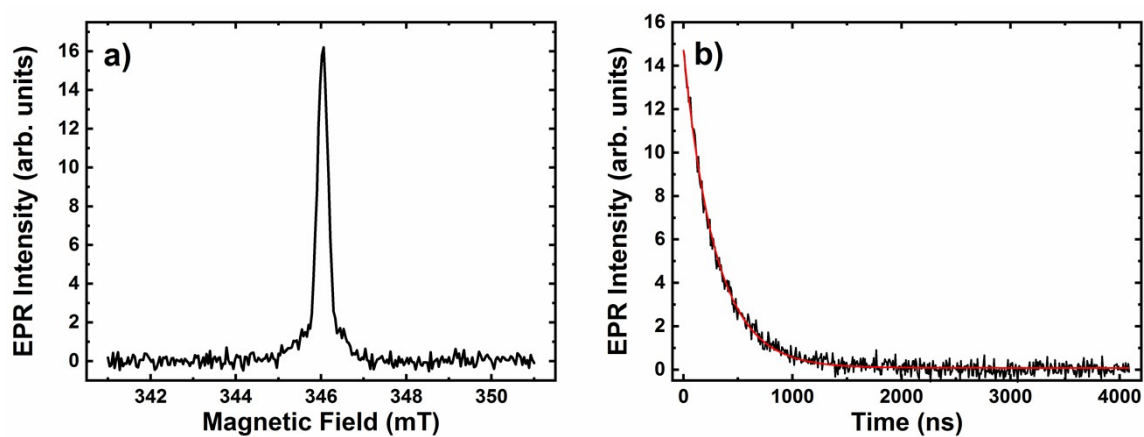
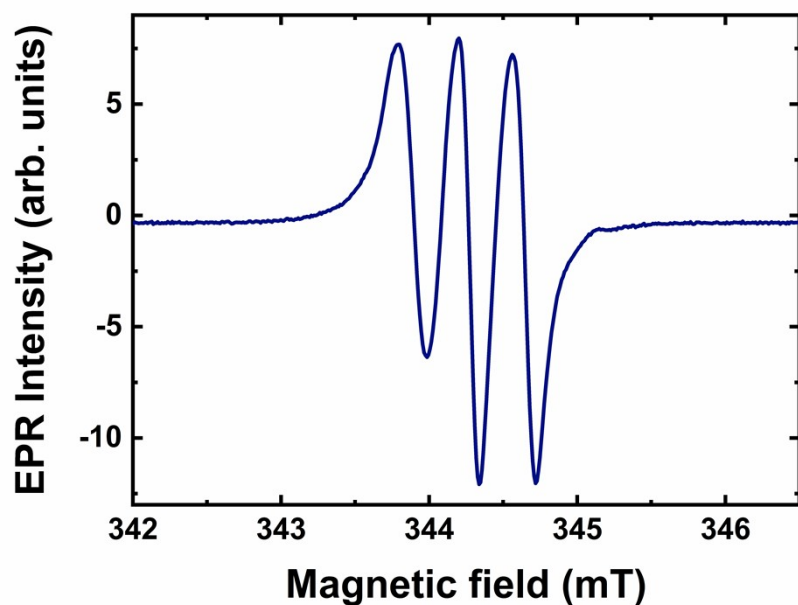
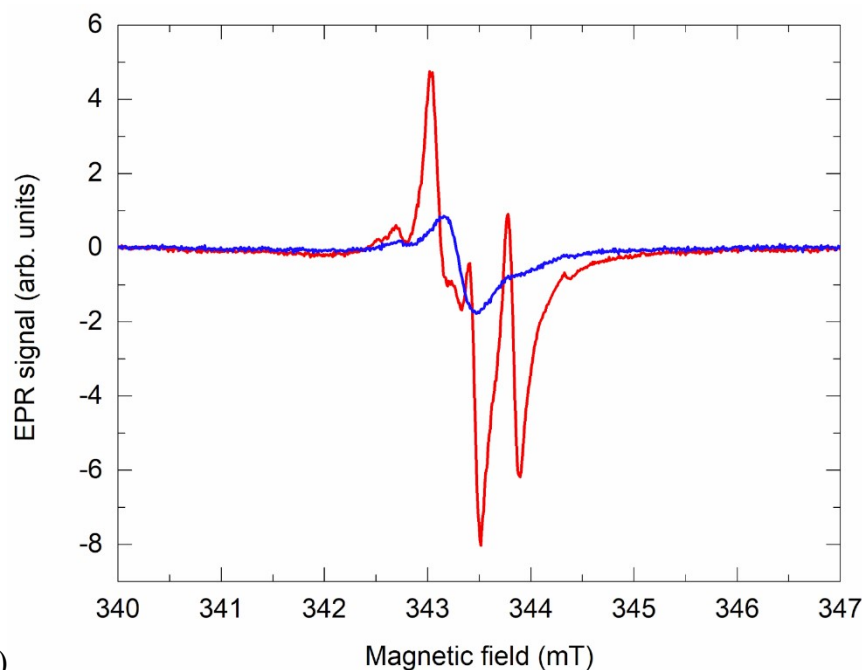


**Figure S4.**

**(a)** Room temperature X-band EPR spectrum of  $g = 2.0022$  component measured with intensity of the echo signal during the field sweep. **(b)** Decay of echo signal as a function of the delay time  $\tau$  between pulses, i.e.,  $\pi/2 - \tau - \pi - \tau$ . Solid red line is a fit to a single exponential decay yielding memory time  $T_M = 296$  ns. Measurements were performed on  $[10]\text{CPP}\supset(\text{C}_{59}\text{N})_2\subset[10]\text{CPP}$  powder previously heated to  $150$  °C for 1 h and then cooled to  $-53$  °C where pulsed EPR experiments were conducted.



(a)



(b)

**Figure S5.**

**(a)** X-band EPR spectrum of  $C_{59}N^{\bullet}$  in [10]CPP measured in a 1-chloronaphthalene frozen at  $-53^{\circ}C$  after the room temperature exposure to UV light (365 nm) for 1 h. The triplet of lines separated by 3.7 G is entirely due to the  $C_{59}N^{\bullet}$  radical. **(b)** Room temperature EPR spectrum in the sample sealed under high vacuum conditions and treated at  $290^{\circ}C$  to create the characteristic  $C_{59}N$  radical signals (red line). The same sample after around 15 minutes open in air (see blue line). While the signal is largely oxidised, nonetheless remnants of the original signal remain, demonstrating again the shielding potential of CPPs.

### Possible reaction of C<sub>59</sub>N• with [10]CPP

Here we explore briefly the possibility that C<sub>59</sub>N• reacts with either its encapsulating [10]CPP, or a [10]CPP neighbour. Since addition of the radical in *para*-position is expected in this case<sup>12</sup> we modelled both concave (internal) and convex (external) covalently bound C<sub>59</sub>N–[10]CPP moieties. In the case of covalent bonding at the concave inside we were not able to obtain even a metastable structure. In all cases the C<sub>59</sub>N• is relaxing back to a location near the center of the CPP-belt. However, binding to the convex outer sphere (corresponding to C<sub>59</sub>N• binding to a neighbouring [10]CPP), there is a metastable minimum (0.12 eV less stable than the separated species) with a covalent bond between the azafullerene and the *para*-site on the [10]CPP, stabilised due to the strain release by the curvature localisation at the sp<sup>3</sup>-C atom (see Fig. S4a). In this case the radical is transferred to the phenyl group, and further delocalised across the neighbouring phenyl units due to their increased planarity in this configuration (Fig. S4b). However, we can exclude such a structure as a source of the lower temperature EPR signal for a number of reasons: Firstly, the species is 0.12 eV less stable than the C<sub>59</sub>N• radical, and a nudged elastic band calculation gives a transition barrier of only 0.39 eV (8.92 kcal/mol) to break the bond. This is easily surmountable at room temperature and means that such an C<sub>59</sub>N–[10]CPP• radical signal should be seen concomitantly with that of C<sub>59</sub>N•, whereas experimentally the signal appears first. Secondly, an equivalent EPR signal from poly(*p*-phenylene), effectively a near-planar CPP structure, shows a linewidth of the X-band EPR signal nearly two orders of magnitude smaller than the current signal.<sup>13</sup> Finally, the extremely low enthalpy barrier and energy difference suggest that entropy will play an important role, since in the non-bonded case both C<sub>59</sub>N• and [10]-CPP are able to near-freely rotate. Thus, we would expect the Gibb's free energy to favour the separated case at room temperature and above, and therefore conclude that the [10]CPP role is structural and does not directly influence the chemical and electronic behaviour of the radical systems.

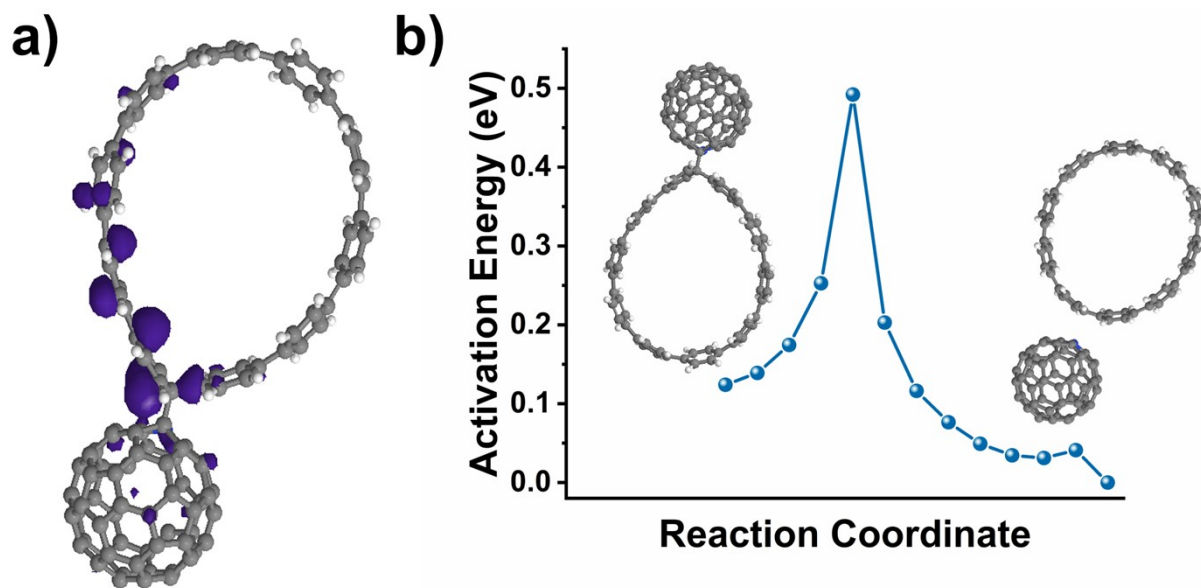


**Figure S6.**

**(a)** C<sub>59</sub>N-[10]CPP, with 1.58 Å C–C covalent bond connecting the azafullerene to the convex exterior of the [10]CPP in *para*-position on a phenyl group. Purple lobes show electronic isosurface for the real part of the unpaired radical electron. **(b)** Calculated reaction barrier for breaking the C-C covalent link.

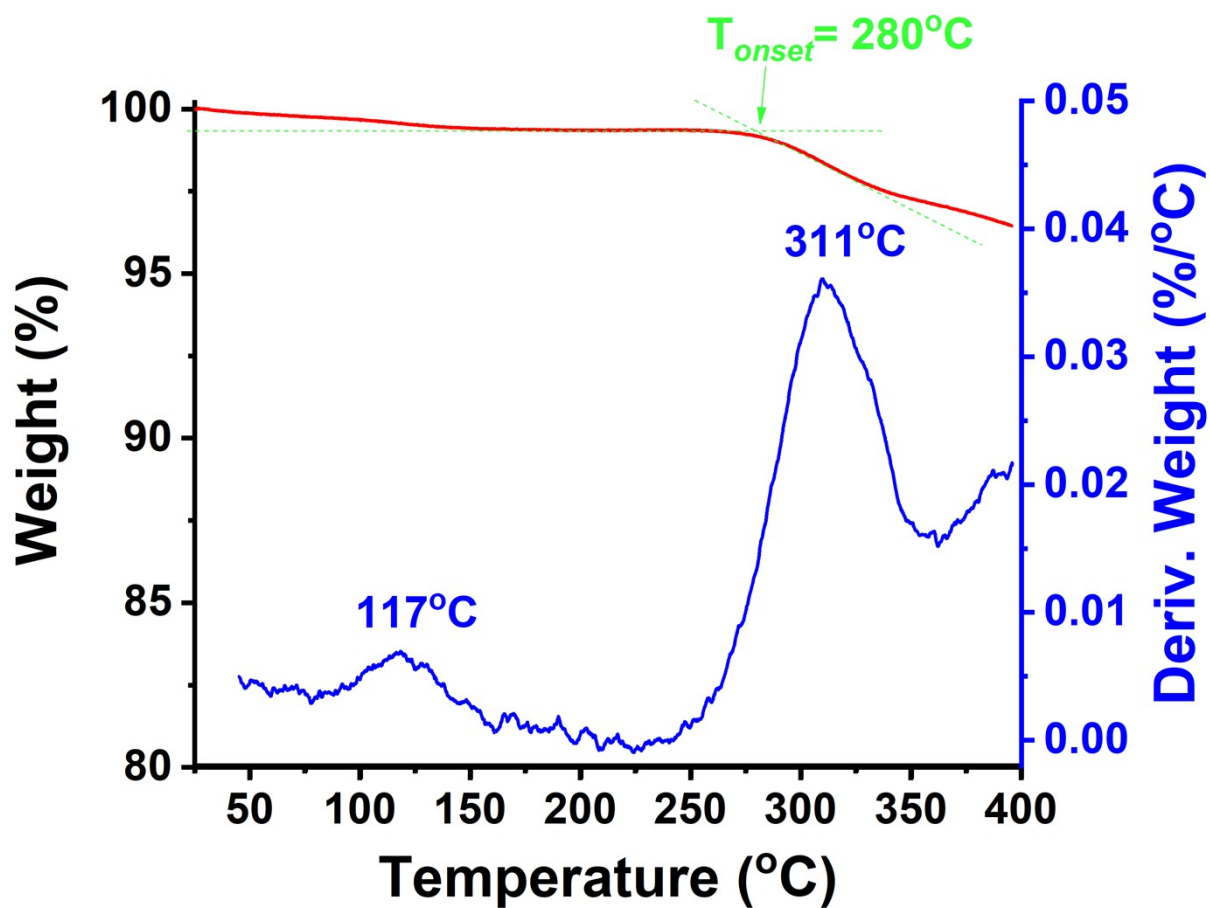
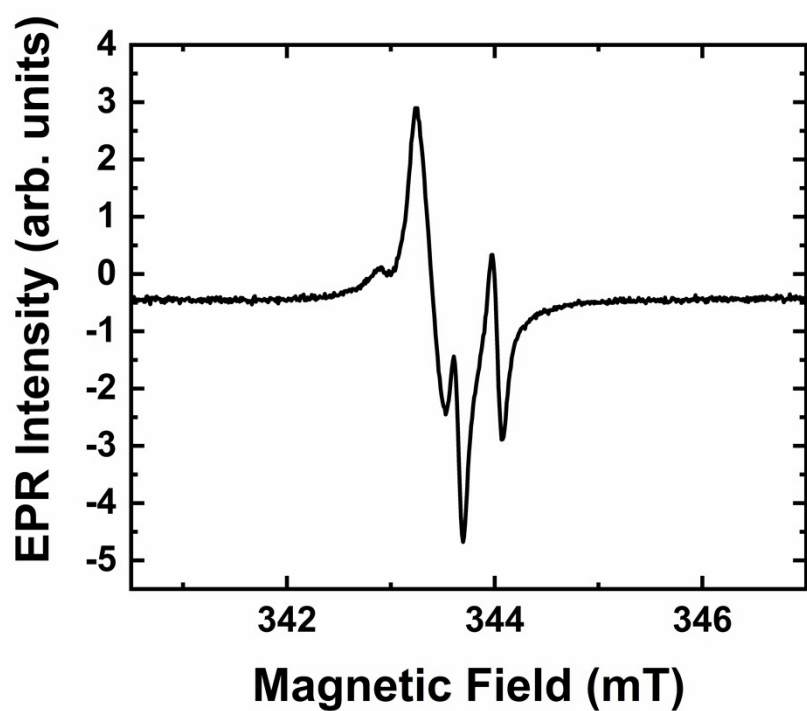


Figure S7.

Thermogravimetric analysis (TGA) curve of the  $[10]CPP \rightleftharpoons (C_{59}N)_2 \rightleftharpoons [10]CPP$  complex, recorded under nitrogen atmosphere.



**Figure S8.**

X-band EPR signal of  $C_{59}N^{\bullet}@[10]CPP$  centers measured at room temperature 30 months after heating the  $[10]CPP \supset (C_{59}N)_2@[10]CPP$  sample to 290 °C.

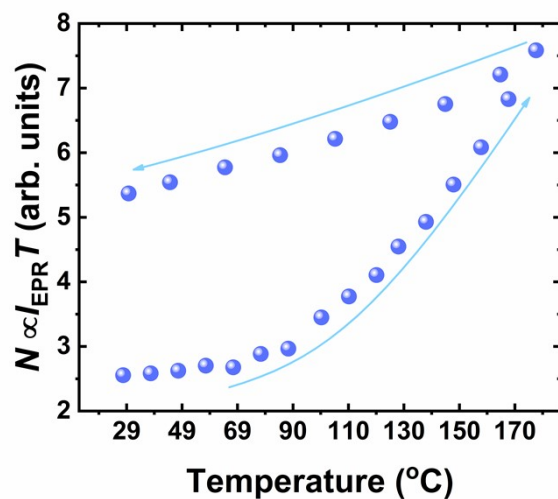


**Figure S9.**

Temperature evolution of the concentration of radical spins contributing to  $g = 2.0022$  signal upon thermal cycling. This particular measurement was performed on a  $[10]\text{CPP}\supset(\text{C}_{59}\text{N})_2\subset[10]\text{CPP}$  powder that initially already showed a weak  $g = 2.0022$  signal.

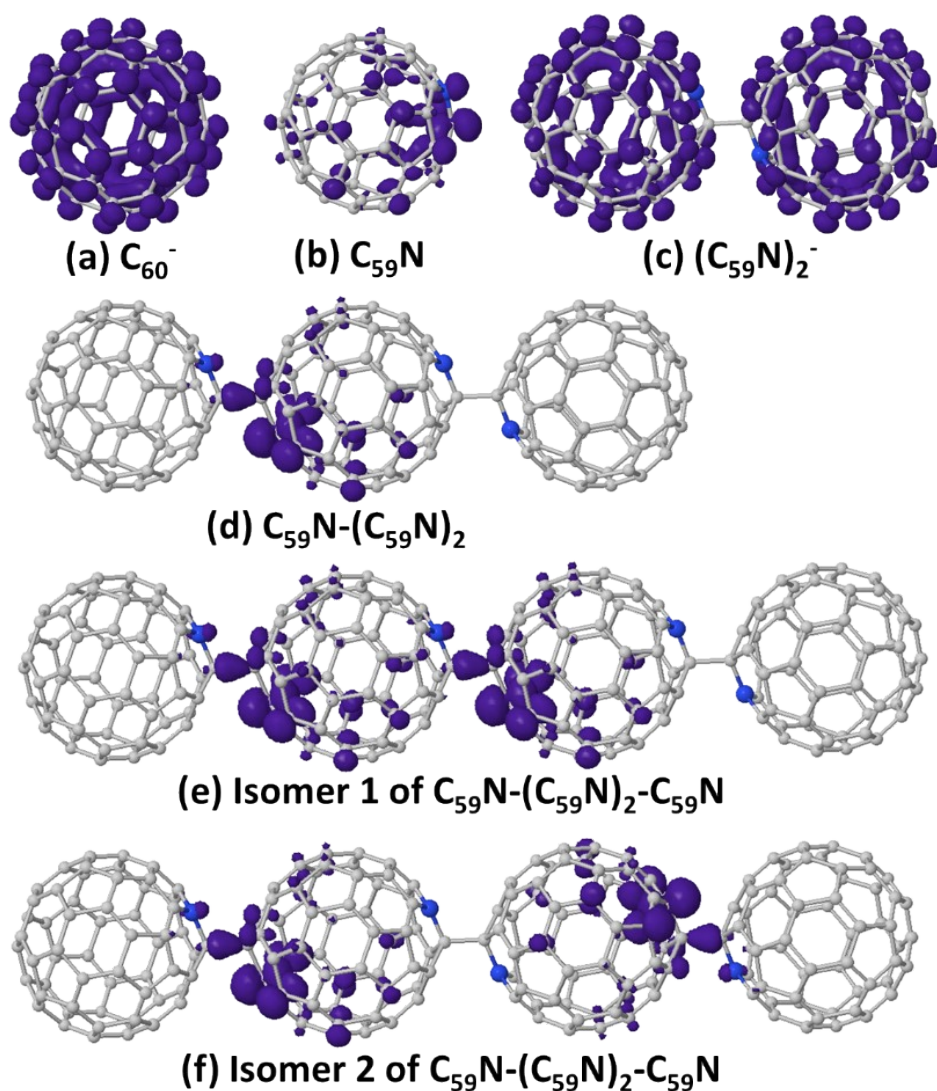


**Figure S10.**

DFT-calculated real-space distribution (wavefunction cut-off of  $0.002e/\text{\AA}^3$ ) of the square of the unpaired spin wavefunction in a variety of azafullerene related species, with  $C_{60}^-$  for comparison. **(a)** possesses averaged spin ( $0\mu_B$ ), **(b-d)** have singlet spin ( $1\mu_B$ ) while **(e-f)** are both triplet ( $2\mu_B$ ) systems. Nitrogen atoms are in blue, carbon in dark grey. Experimentally these species will be encapsulated within [10]CPP.

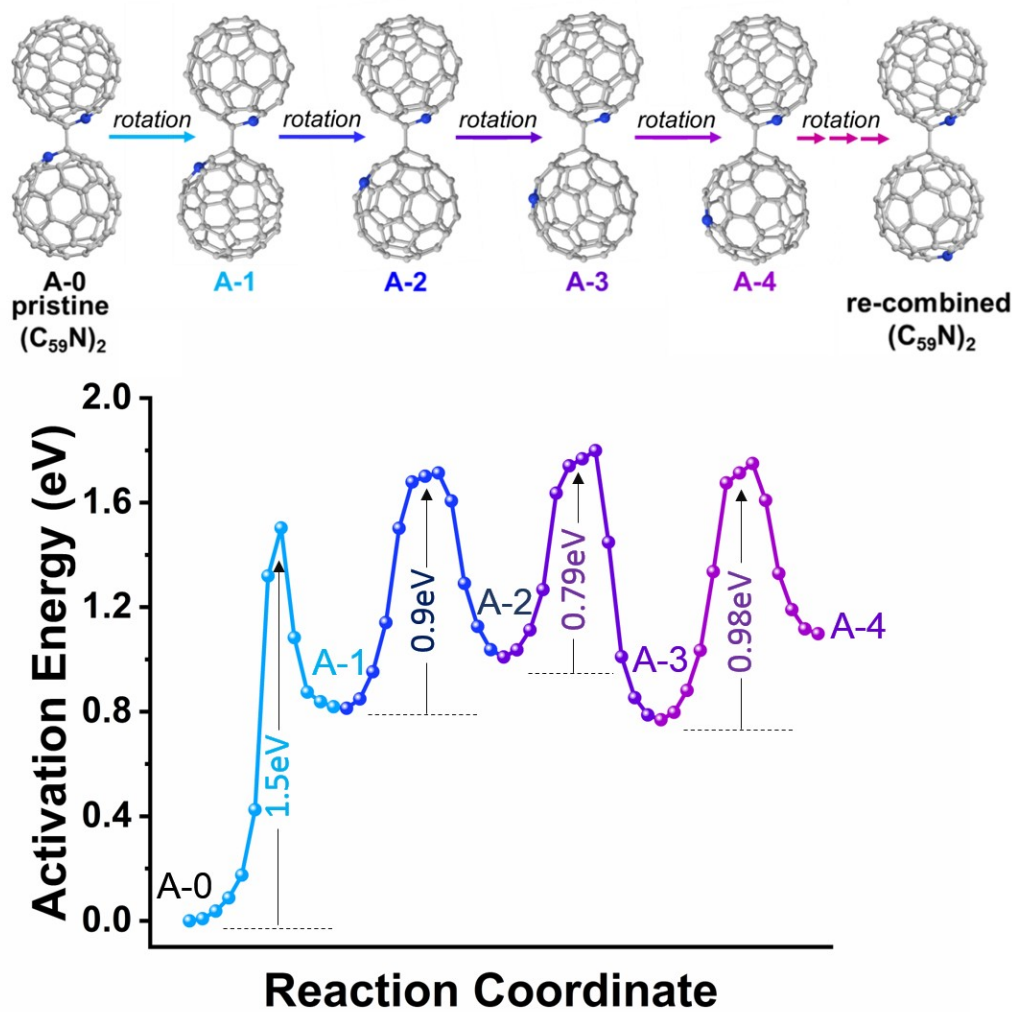


**Figure S11.**

Calculated barriers to rotate one fullerene cage in  $(C_{59}N)_2$ . Labels A- $n$  indicate the interfullerene bond between atom A and atom  $n$ ,  $n=0 \rightarrow 4$ , atom sites referring to the azafullerene figure on the right, towards backbonding dimer. A-0 indicates the stable ground-state  $(C_{59}N)_2$  azafullerene dimer.

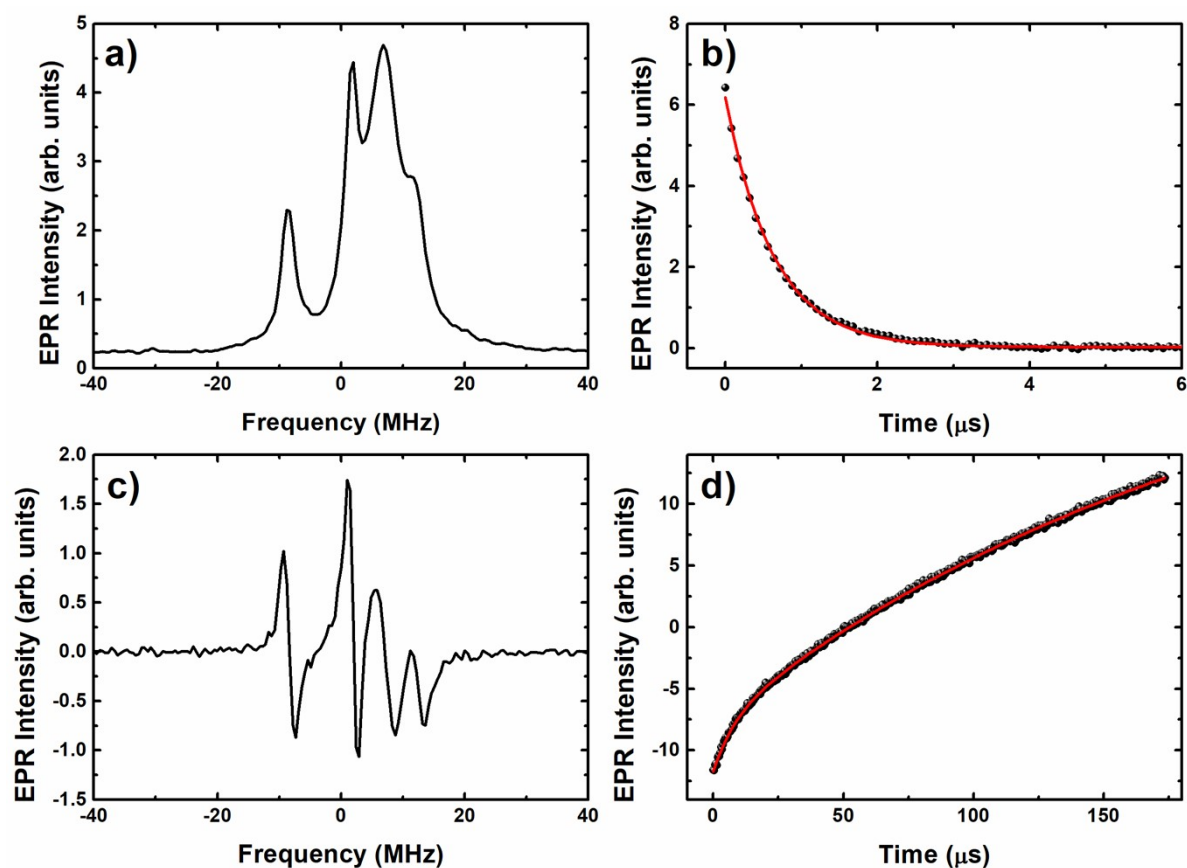


**Figure S12.**

(a) Fourier transform of the spin echo signal measured at room temperature for [10]CPP-(C<sub>59</sub>N)<sub>2</sub>-[10]CPP powder previously heated to 290 °C. The spectrum is dominated by the triplet of peaks associated with the C<sub>59</sub>N•-[10]CPP radical and the  $g = 2.0022$  peak. (b) Echo decay as a function of the delay time (black dots) yielding the memory time  $T_M = 631$  ns (red line is a fit to a single exponential decay). (c) Derivative of the spectrum shown in (a) displaying individual components analogous to the continuous-wave EPR spectrum (Fig. 1b). (d) Measurement of the magnetization curve (black dots) with the inversion recovery technique yielding spin-lattice relaxation times  $T_{1a} = 8.1$  μs and  $T_{1b} = 210$  μs after a two-exponential fit (solid red line).

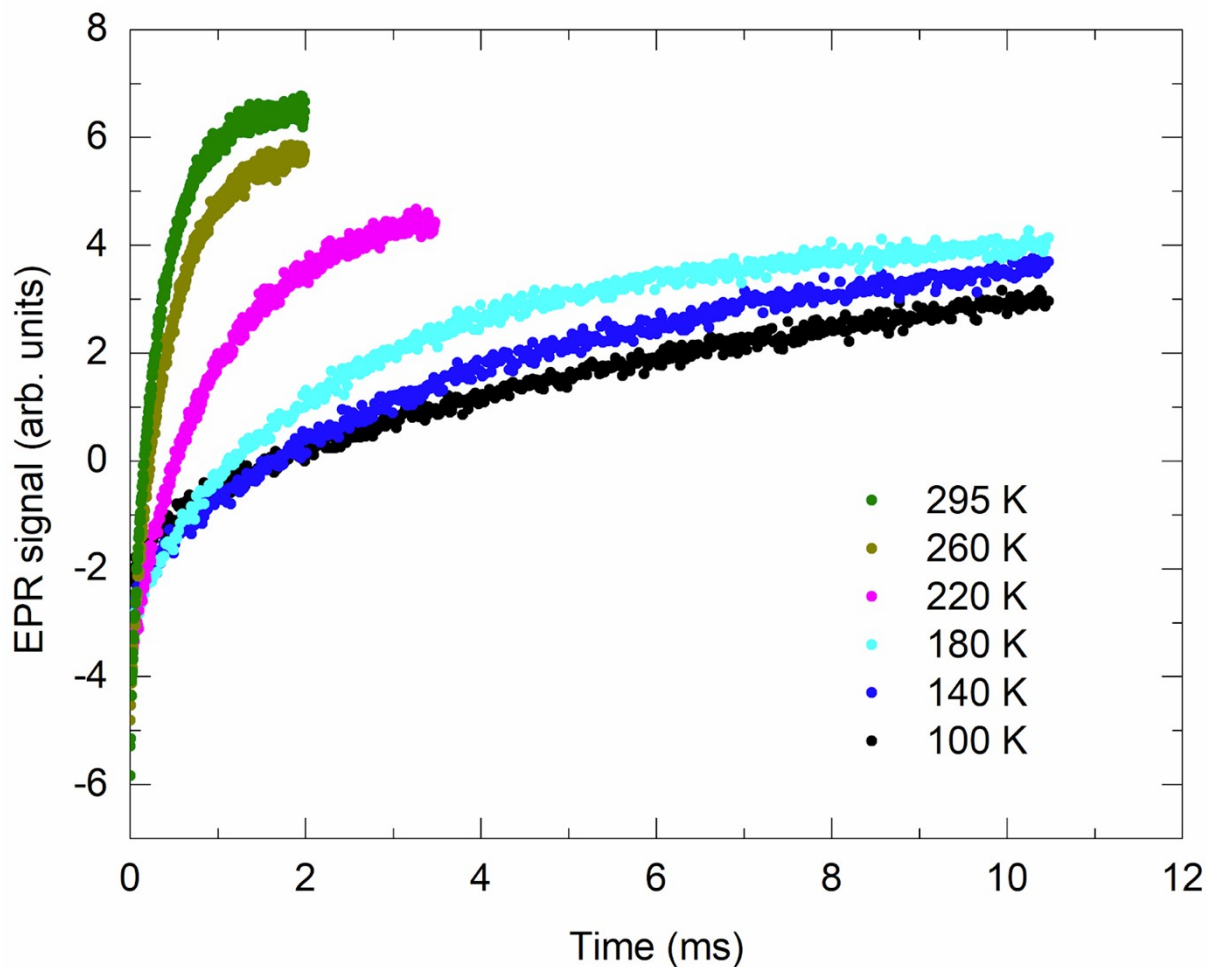


**Figure S13.** Temperature dependent measurements of the spin-lattice relaxation time,  $T_1$ . Even without trying to fit the data, it is clear that relaxation times become extremely long on cooling. For example, at 180 K,  $T_1$  is already 2.89(6) ms. On further cooling it becomes so long that it can no longer be reliably determined with our pulsed EPR spectrometer as it approaches the range of almost seconds. Thus, the coherence times of  $C_{59}N$ -CPP centers are extremely long at cryogenic temperatures.

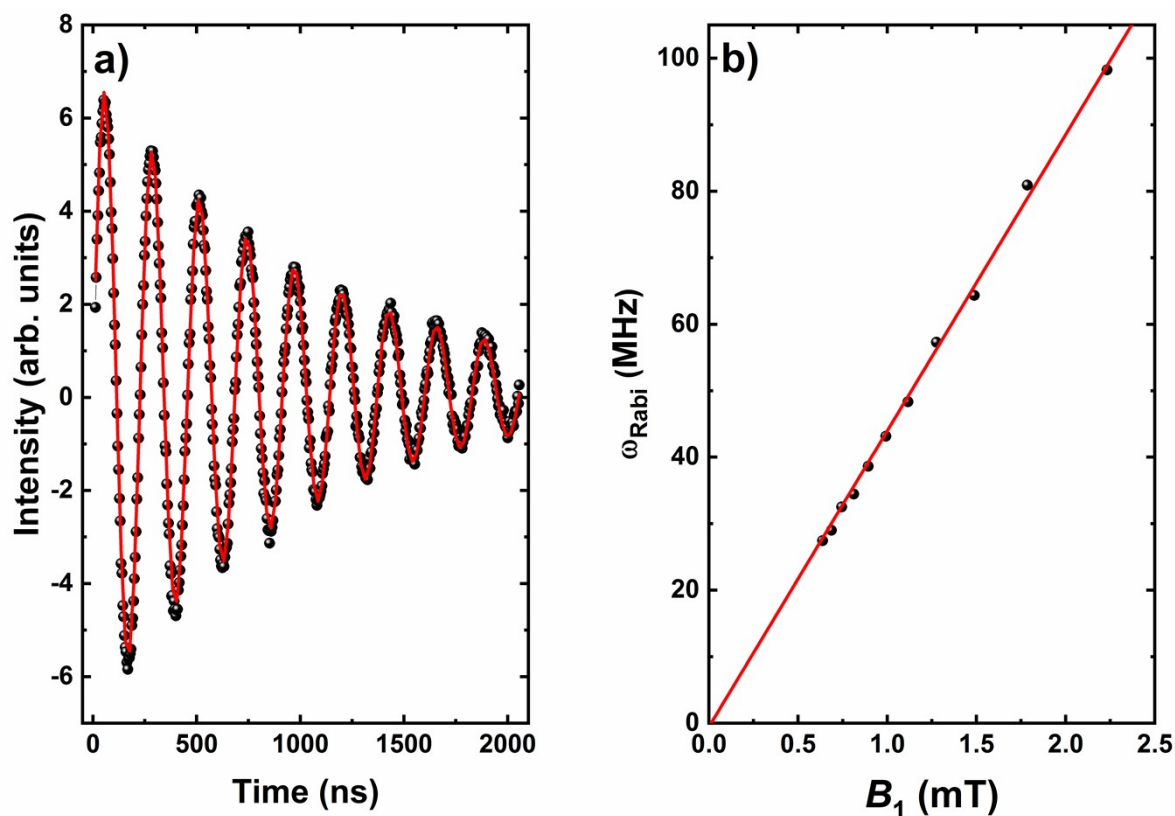


**Figure S14.**

**(a)** The electron spin Rabi oscillations (black spheres) measured as a function of the nutation pulse length time,  $\tau_p$ , for the  $\text{C}_{59}\text{N}^{\bullet}\text{C}[10]\text{CPP}$  radical at the position of  $m_I = +1$  line (Figure S7a, low frequency line). The measurement was performed at room temperature on the powder previously annealed at 290 °C. The solid red line is a fit to a damped cosine oscillation  $S(\tau_p) = S_0 \cos(\omega_{\text{Rabi}}\tau_p + \phi_0) \exp[-\tau_p/T_m]$ , yielding the Rabi frequency  $\omega_{\text{Rabi}}$ . **(b)** The linear dependence of the Rabi frequency on the driving microwave field is a clear and direct proof of the coherent manipulation of the electronic spin state.

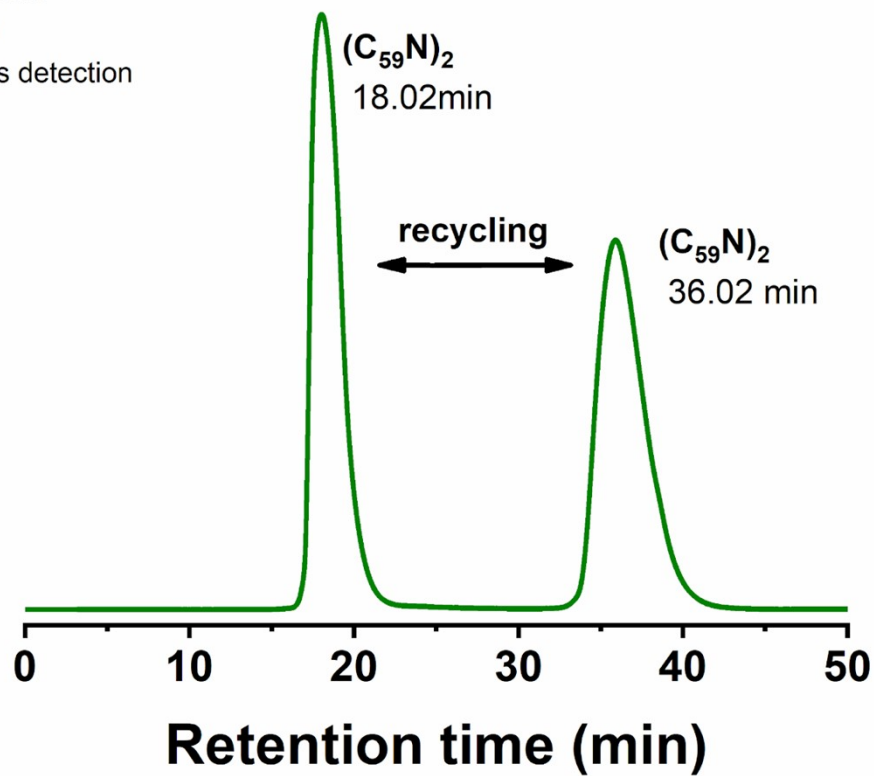
**Figure S15.** HPLC Trace from  $(C_{59}N)_2$  purification showing absence of any residual  $C_{60}$  impurities (which would be expected at around 8 minutes retention time).

Buckyprep preparative column 20x250 mm

20ml/min flow rate

toluene eluent

335 nm UV-Vis detection



<b>C<sub>59</sub>N</b>		
<b>Atom species</b>	<b>Atom</b>	<b>A<sub>iso</sub> (MHz)</b>
<sup>14</sup> N	9	10.76 (11.50)
<sup>13</sup> C	11	47.82 (47.91)
	10	-3.13 (-2.62)
	20	-3.13 (-2.62)

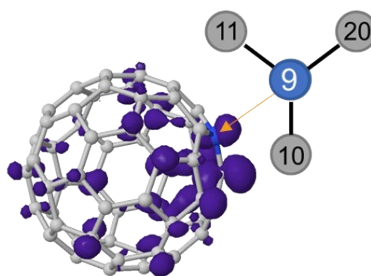


**Table S1-1.**

Calculated DFT isotropic Hyperfine Coupling Parameter,  $A_{\text{iso}}$  (MHz) for atom sites in C<sub>59</sub>N radical species, using the local density approximation (LDA) and generalised gradient approximation (GGA) (in brackets). Schematics show the atomic numbering used in the table, Carbon atoms marked in Grey, Nitrogen in Blue.

$(C_{59}N)_2^-$		
Atom species	Atom	$A_{iso}$ (MHz)
$^{14}N$	9	-0.42 (-0.36)
	117	-0.42 (-0.36)
$^{13}C$	10	2.24 (2.77)
	20	2.24 (2.77)
	103	2.24 (2.76)
	118	2.24 (2.76)
	11	-1.17 (-0.93)
	120	-1.16 (-0.93)

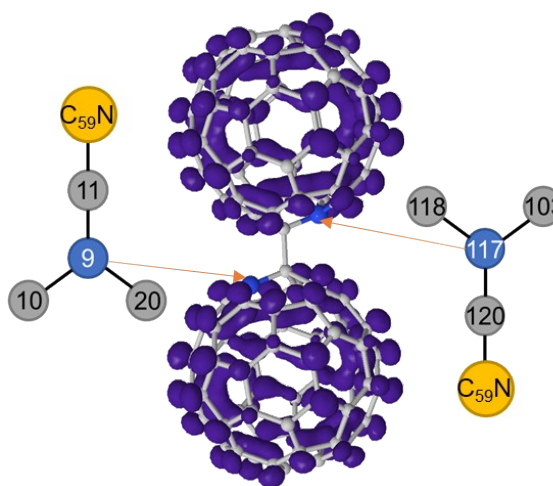


**Table S1-2.**

Calculated DFT isotropic Hyperfine Coupling Parameter,  $A_{iso}$  (MHz) for atom sites in  $(C_{59}N)_2^-$  radical species, using the local density approximation (LDA) and generalised gradient approximation (GGA) (in brackets). Schematics show the atomic numbering used in the table, Carbon atoms marked in Grey, Nitrogen in Blue.

$C_{60}^-$		
Atom species	Atom	$A_{iso}$ (MHz)
$^{13}C$	6	2.26 (3.82)
	13	2.26 (3.81)
	1	2.21 (3.74)
	12	2.20 (3.73)
	2	2.19 (3.71)
	19	2.16 (3.66)
	3	2.15 (3.66)
	11	2.15 (3.67)
	27	2.15 (3.63)
	35	2.15 (3.63)

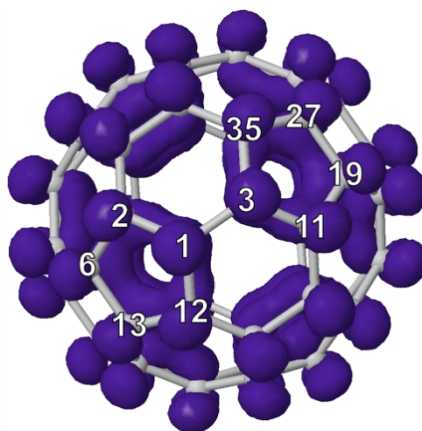


**Table S1-3.**

Calculated DFT isotropic Hyperfine Coupling Parameter,  $A_{iso}$  (MHz) for atom sites in  $C_{60}^-$  radical species, using the local density approximation (LDA) and generalised gradient approximation (GGA) (in brackets). Schematics show the atomic numbering used in the table, Carbon atoms marked in Grey, Nitrogen in Blue.

$C_{59}N-(C_{59}N)_2$		
Atom Species	Atom	$A_{iso}$ (MHz)
$^{14}N$	129	1.91 (2.15)
	9	0.37 (0.27)
	117	-0.02 (-0.05)
$^{13}C$	57	78.86 (117.88)
	131	77.41 (80.44)
	43	-24.92 (-40.24)
	58	-24.92 (-40.24)
	60	-12.05 (-18.00)
	120	4.10 (4.26)
	10	-1.36 (-2.64)
	20	-1.36 (-2.64)
	11	-1.32 (-1.95)
	130	-0.53 (-0.37)
	140	-0.53 (-0.37)
	103	0.00 (0.02)
	118	0.00 (0.02)

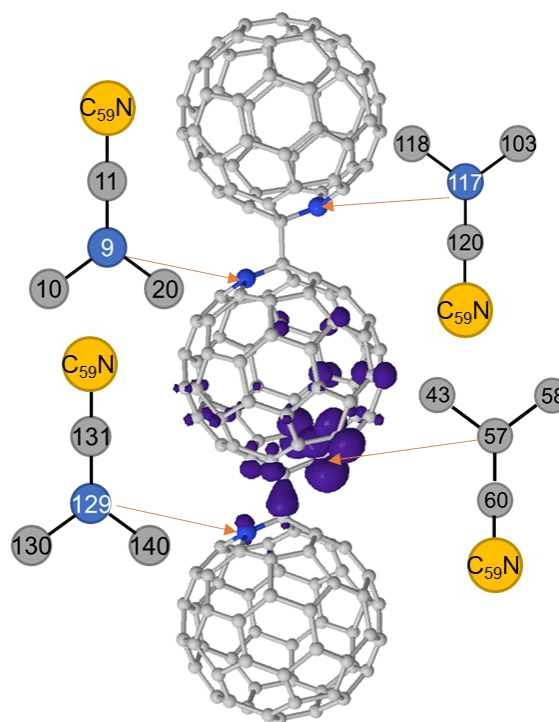


**Table S1-4.**

Calculated DFT isotropic Hyperfine Coupling Parameter,  $A_{iso}$  (MHz) for atom sites in  $C_{59}N-(C_{59}N)_2$  radical species, using the local density approximation (LDA) and generalised gradient approximation (GGA) (in brackets). Schematics show the atomic numbering used in the table, Carbon atoms marked in Grey, Nitrogen in Blue.

$C_{59}N-C_{59}N-(C_{59}N)_2$		
Atom Species	Atom	$A_{iso}$ (MHz)
$^{14}N$	152	1.26 (1.36)
	212	0.97 (1.10)
$^{13}C$	151	39.50 (59.06)
	57	39.46 (58.87)
	209	39.03 (40.49)
	149	38.60 (39.71)
	161	10.72 (14.32)
	139	10.70 (14.32)
	44	10.61 (14.17)
	56	10.60 (14.17)
	150	-6.06 (-9.07)
	60	-3.59 (-6.57)
	159	-0.93 (-1.47)
	142	-0.92 (-1.46)
	201	-0.26 (-0.17)
	219	-0.25 (-0.16)

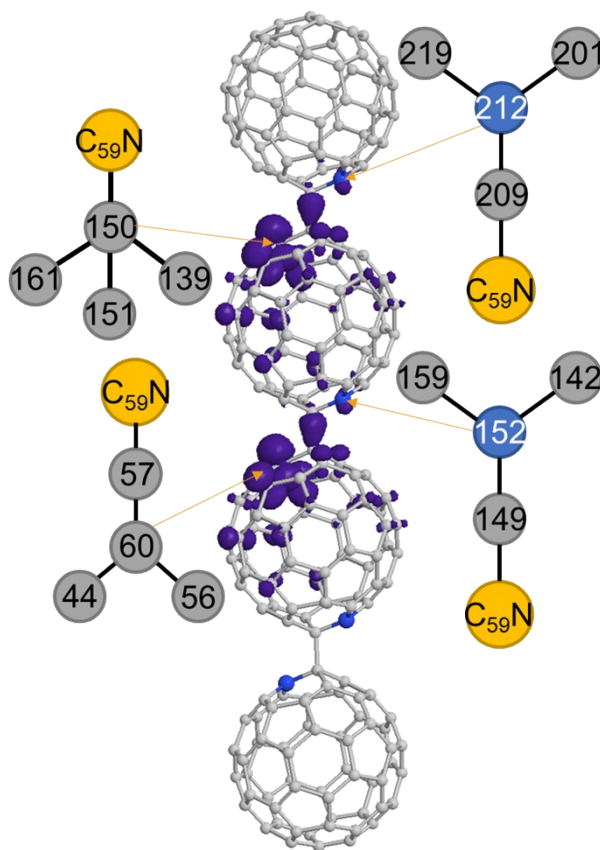


**Table S1-5.**

Calculated DFT isotropic Hyperfine Coupling Parameter,  $A_{iso}$  (MHz) for atom sites in  $C_{59}N-C_{59}N-(C_{59}N)_2$  radical species, using the local density approximation (LDA) and generalised gradient approximation (GGA) (in brackets). Schematics show the atomic numbering used in the table, Carbon atoms marked in Grey, Nitrogen in Blue.

### Estimation of the coupling between qubits

The coupling term between qubits will have a function of the form (**Equation 1**).

$$H = J S_1 S_2 . \quad (1)$$

If the coupling strength,  $J$  is assumed to be due to the dipolar interaction between the two centers, this gives **Equation 2**

$$J = \frac{\mu_0 \hbar \Gamma^2}{2r^3} = 52 \text{ MHz}/r^3, \quad (2)$$

(where  $r$  is given in nm). Assuming  $r = 1.7$  nm (twice the diameter of  $C_{60}$  plus a 0.3 nm inter-fullerene spacing) this gives  $J \sim 10$  MHz.

## References

- (1) Gaita-Ariño, A.; Luis, F.; Hill, S.; Coronado, E. Molecular Spins for Quantum Computation. *Nature Chemistry* **2019**, *11* (4), 301–309. <https://doi.org/10.1038/s41557-019-0232-y>.
- (2) Clemente-Juan, J. M.; Coronado, E.; Gaita-Ariño, A. Magnetic Polyoxometalates: From Molecular Magnetism to Molecular Spintronics and Quantum Computing. *Chem. Soc. Rev.* **2012**, *41* (22), 7464. <https://doi.org/10.1039/c2cs35205b>.
- (3) Aromí, G.; Aguilà, D.; Gamez, P.; Luis, F.; Roubeau, O. Design of Magnetic Coordination Complexes for Quantum Computing. *Chem. Soc. Rev.* **2012**, *41* (2), 537–546. <https://doi.org/10.1039/C1CS15115K>.
- (4) Brown, C. M.; Cristofolini, L.; Kordatos, K.; Prassides, K.; Bellavia, C.; González, R.; Keshavarz-K., M.; Wudl, F.; Cheetham, A. K.; Zhang, J. P.; Andreoni, W.; Curioni, A.; Fitch, A. N.; Pattison, P. On the Crystal Structure of Azafullerene (C59N)<sub>2</sub>. *Chem. Mater.* **1996**, *8* (11), 2548–2550. <https://doi.org/10.1021/cm960354i>.
- (5) Sessoli, R. Magnetic Molecules Back in the Race. *Nature* **2017**, *548* (7668), 400–401. <https://doi.org/10.1038/548400a>.
- (6) Tagmatarchis, N.; Shinohara, H.; Pichler, T.; Krause, M.; Kuzmany, H. Electronic Absorption and Vibrational Spectroscopy of Azafullerene C59HN and Its Oxide C59HNO. *J. Chem. Soc., Perkin Trans. 2* **2000**, No. 12, 2361–2362. <https://doi.org/10.1039/B007865O>.
- (7) Huang, Q.; Zhuang, G.; Zhang, M.; Wang, J.; Wang, S.; Wu, Y.; Yang, S.; Du, P. A Long  $\pi$ -Conjugated Poly(Para-Phenylene)-Based Polymeric Segment of Single-Walled Carbon Nanotubes. *J. Am. Chem. Soc.* **2019**, *6*.
- (8) Chen, H.; Golder, M. R.; Wang, F.; Jasti, R.; Swan, A. K. Raman Spectroscopy of Carbon Nanohoops. *Carbon* **2014**, *67*, 203–213. <https://doi.org/10.1016/j.carbon.2013.09.082>.
- (9) Joung, S.-K.; Okazaki, T.; Okada, S.; Iijima, S. Interaction between Single-Wall Carbon Nanotubes and Encapsulated C60 Probed by Resonance Raman Spectroscopy. *Phys. Chem. Chem. Phys.* **2010**, *12* (28), 8119–8123. <https://doi.org/10.1039/C000102C>.
- (10) Kim, K.-C.; Hauke, F.; Hirsch, A.; Boyd, P. D. W.; Carter, E.; Armstrong, R. S.; Lay, P. A.; Reed, C. A. Synthesis of the C59N<sup>+</sup> Carbocation. A Monomeric Azafullerene Isoelectronic to C60. *J Am Chem Soc* **2003**, *125* (14), 4024–4025. <https://doi.org/10.1021/ja034014r>.
- (11) Barich, D. H.; Pugmire, R. J.; Grant, D. M.; Iulicucci, R. J. Investigation of the Structural Conformation of Biphenyl by Solid State <sup>13</sup>C NMR and Quantum Chemical NMR Shift Calculations. *J. Phys. Chem. A* **2001**, *105* (28), 6780–6784. <https://doi.org/10.1021/jp004314k>.
- (12) Kayahara, E.; Qu, R.; Yamago, S. Bromination of Cycloparaphenylenes: Strain-Induced Site-Selective Bis-Addition and Its Application for Late-Stage Functionalization. *Angewandte Chemie International Edition* **2017**, *56* (35), 10428–10432. <https://doi.org/10.1002/anie.201704982>.
- (13) Qing Jin, C.; Kun Wang, L.; An Liu, Y. Magnetic Resonance Experiments on Undoped and Doped Poly(Para-Phenylene). *Synthetic Metals* **1992**, *49* (1), 261–265. [https://doi.org/10.1016/0379-6779\(92\)90098-4](https://doi.org/10.1016/0379-6779(92)90098-4).